Experimental tests on Crescent Shaped Braces hysteretic devices

Experimental tests on Crescent Shaped Braces hysteretic devices

Michele Palermo, Luca Pieraccini [(1)], Antoine Dib, Stefano Silvestri, and Tomaso Trombetti
Department DICAM, University of Bologna, Viale Risorgimento 2, 40136 Bologna, Italy

Abstract

Crescent Shaped Braces, CSBs, are steel hysteretic devices which, thanks to their geometrical configuration, are characterized by an enhanced seismic behavior that makes them a promising alternative to conventional diagonal steel braces and other seismic devices such as Buckling Resisting Braces and Scorpions. The present work reports the results of the first experimental campaign devoted to assess the cyclic experimental behavior of CSBs. The main goals of the experimental campaign are: (i) to verify/compare the effectiveness of design formulas for the seismic design of CSB introduced by the authors in a previous research work and the predictions of a simplified non-linear model in terms of force-displacement envelop response; (ii) to assess the experimental non-linear cyclic behavior in terms of ductility capacity, energy dissipation capacity, failures.

1. Introduction

Energy dissipation systems for the mitigation of the seismic-induced effects have been developed over the last half century in order to raise seismic performance levels of constructions keeping costs reasonable (Christopoulos et al. 2006). They are usually classified in three main categories: active, semi-active and passive systems. Active and semi-active control systems are force delivery devices integrated with real-time processing evaluators/controllers and sensors within the structure (Soong and Spencer 2002). Such systems require external power sources, which represents a significant limitation on their seismic applicability. Passive systems operate without external power supply and are activated by the motion (displacements and/or velocities) of the structure. Metallic and friction (hysteretic) dampers belong to the category of displacement-activated supplemental damping systems. Steel dampers take advantage of the hysteretic behavior of the material exceeding its yielding point. Particularly desirable properties of these devices are a stable hysteretic behavior, the ability in sustaining an adequate number of cyclic loading-unloading (low-cycle fatigue), long term reliability and low sensitivity to environmental temperature (Soong and Spencer 2002).

Since the mid-1970s, a considerable number of hysteretic devices have been developed and tested. According to Christopoulos et al. (2006), the ones that have demonstrated a particularly desirable behavior

[1] Corresponding author. Phone: +39 051 20 9 3232; Fax: +39 051 20 9 3236; e-mail: luca.pieraccini5@unibo.it

are here briefly recalled. The Added Damping – Added Stiffness (ADAS) device, originally manufactured by Bechtel Corporation in the 1980s, is usually installed between the apex of a chevron brace and the underside of the beam. The Triangular Added Damping – Added Stiffness (TADAS) device, developed by Tsai et al. (1993), is a variation of the original ADAS device which makes use of triangular plates as dissipative steel elements. In the mid-1970s, Lead Extrusion Devices (LED) were proposed in New Zeland (Robinson and Greenbank 1976) taking advantage of the stable and repeatable hysteretic behavior of a lead element. The Buckling Restrained Brace (BRB), as the unbounded brace manufactured by Nippon Steel Corporation in the early 1980s, consists in a steel member encased in a tube filled with concrete that prevents the buckling (Black et al. 2004). The Cast Steel Yielding Fuse (CSF) device, as the one manufactured by Cast Connex Corporation (under the commercial name of Scorpion Yielding Devices), is a steel device for concentrically braced frames that dissipates energy through inelastic flexural yielding of special elements. The system exhibits a full, symmetric hysteresis characterized by an increase in stiffness at brace elongations larger than the design level. This increase in stiffness is a result of the second-order change in geometry of the yielding fingers, each of which is shaped to promote the spread of plasticity along its entire length. This effect can limit peak drifts and residual drifts and mitigate the likelihood that, in the event of a large earthquake, the inelastic demand will collect at a single story (Gray et al. 2010 and Gray et al. 2014). Recently, a wide experimental campaign aimed at assessing the effectiveness of two Energy Dissipating Bracing (EDB) has been carried out at the University of Basilicata (project JetPacs) (Di Cesare et al. 2012). In detail, the two EDB systems are: the Hysteretic Damper (HD) device and the visco-recentring device (so called SMA+VD). The HD devices are composed by ad hoc shaped steel plates in order to dissipate energy through flexural yielding and characterized by an elastic-plastic with hardening force-displacement response. The SMA+VD devices consist of the coupling of fluid viscous velocity-dependent energy-dissipating devices (VD) with a displacement dependent Ni–Ti shape memory alloy device (SMA), which are characterized by a symmetric flag-shaped force-displacement response.

In 2009, within the framework of Stiffness-Strength-Ductility design (a design procedure base on PBSD approach), some of the authors introduced a new hysteretic device, known as Crescent Shaped Brace (CSB), able to fulfill multiple seismic design objectives in terms of stiffness, strength and ductility and represented by mean of an objective curve (Trombetti et al. 2009). Later on, the potential capabilities of CSB devices has been shown through an applicative example where a five-storey steel frame is designed according to the concept of “enhanced first storey isolation” inspired to the original concept of storey isolation proposed in the late 1960s (Fintel and Khan 1968). The CSB devices placed at the ground floor, thanks to their peculiar geometrical shapes, are characterized by a lateral stiffness uncoupled from the yield strength and by an overall symmetric hysteretic behavior with a hardening response at large drifts (due to non-linear geometrical effects) which may prevent from global structural instability due to second-order effects (such as P-Δ effects).

In a more recent research work (Palermo et al. 2015) the attention has been devoted in the study of the single device. Analytical and numerical studies devoted to the assessment of the non-linear mechanical and geometrical behavior of CSB have been developed, with a particular attention devoted to seismic design purposes. To complete the seismic assessment of the device, experimental tests on various scaled specimens have been carried out at the Structural Engineering and Geotechnical Laboratory (LISG) of the University of Bologna (Italy). In the present work, the main results of the experimental tests are presented.

2. The seismic behavior of Crescent Shaped Braces

2.1 The geometrical and mechanical properties of CSBs

The Crescent Shaped Brace (CSB) is a hysteretic steel device made by commercial steel profiles connecting two points of the structure (i.e. two consecutive stories when used as diagonal braces in framed structure). Based on their configuration and placement inside the frame structure, two global force-displacement responses could be typically observed: (i) asymmetric response of the single bilinear CSB device (Figure 1a); (ii) symmetric response of the couple of two bilinear CSB devices (Figure 1b).

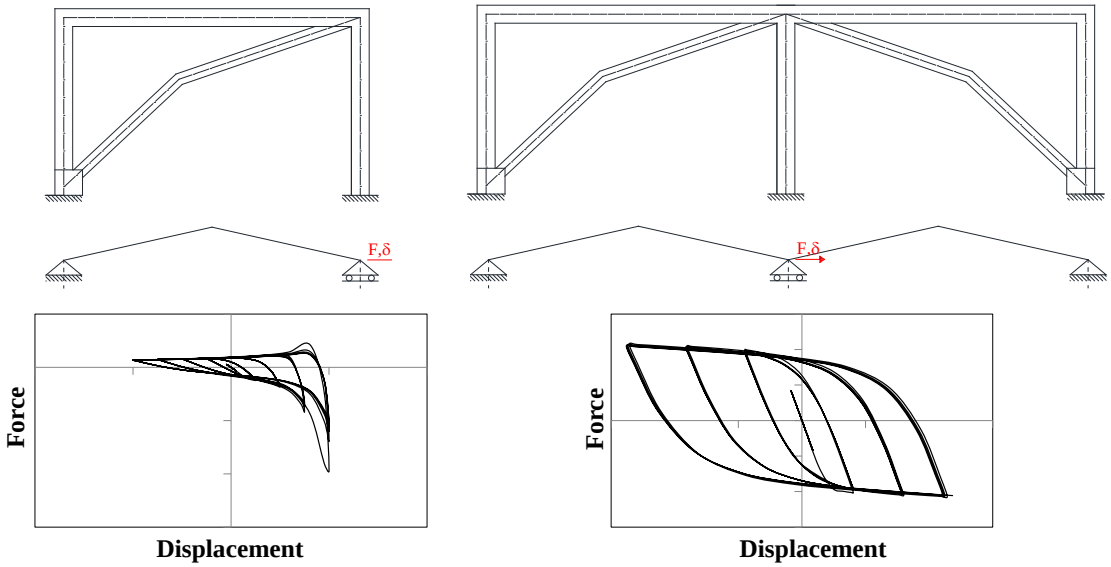

(a) (b)

Figure 1 – (a) A bilinear CSB device inserted in a frame and its asymmetric force-displacement response; (b) two mirrored disposed bilinear CSB devices inserted in two frames and their symmetric force-displacement response. (Adapted from Palermo et al. 2015).

The hysteretic force-displacement response of the single CSB device is strongly asymmetric due to non-linear geometrical effects: significant hardening response under lateral loads inducing tension in the brace, softening response under lateral loads inducing compression in the braces (Figure 1a). On the contrary, two CSB devices inserted in a two span frame structure as displayed in Figure 1b are characterized by an overall symmetric hysteretic response, given that one works in compression, whilst the other one works in tension. Such a global response remembers the desirable behavior of the Scorpion Yielding Device (see Figure 10 of Gray et al. 2014). With reference to Figure 2, the relevant geometrical and mechanical properties of a bilinear CSB device are listed below.

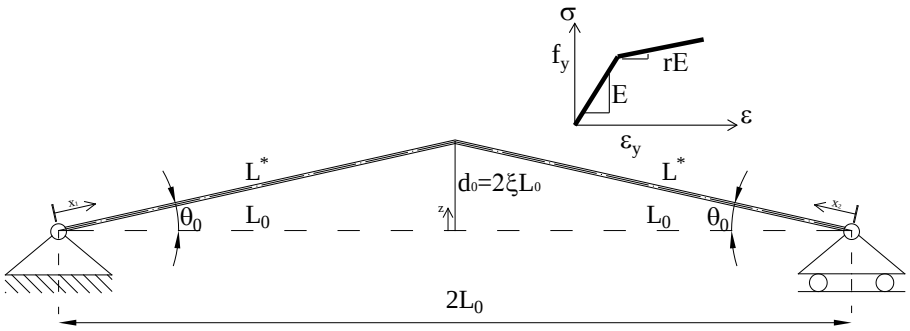

Figure 2 – The geometry of a bilinear CSB device (Adapted from Palermo et al. 2015).

Geometrical properties of the single device in the initial configuration:

- length of each straight member L^*;
- inclination with respect to the horizontal direction θ_0 (L_0 indicates the horizontal projection of L^*);
- lever arm d_0, or its normalized version $\xi = d_0/2L_0$.
- cross-section height h.
- cross-section area A.
- in-plane and out-of-plane moment of inertia of the cross-section J and *I*, respectively.

Mechanical material properties (assuming a bilinear elastic-plastic stress–strain relationship):

- elastic modulus *E*;
- yield strength f_y;
- hardening ratio, *r*, as defined as the E_p/E ratio, where E_p is the tangent of the stress–strain curve after the yielding point.

2.2 The seismic design of frame structures equipped with CSBs

In previous research works by some of the authors, the mechanical behaviors of both a single device as subjected to cyclic lateral forces (Palermo et al. 2015) and a frame structure equipped with CSBs (Palermo et al. 2014) were investigated.

In detail, in the work by Palermo et al. (2015) the attention was mainly focused in the study of the elastic behavior up to the first yielding of a single bilinear CSB system subjected to a lateral load. In particular, analytical expressions of the initial lateral stiffness and lateral force leading to the first yielding has been derived studying the equilibrium in the initial undeformed configuration considering both the axial and flexural contributions to the total elastic deformation. It has been recognized that the contribution of the axial deformability can be neglected for values of normalized lever arm $\xi > 0.1$. In such a case, the following simplified analytical expressions of the lateral stiffness K_{L0} and lateral force leading to the first yielding F_{y0}

can be used for design purposes (in the following, the subscript *0* indicates that the quantities are evaluated with respect to the initial undeformed configuration):

$$K_{L0} = \frac{3}{2}\frac{EJ}{L^{*3}\sin^2\theta_0} \tag{1}$$

$$F_{y0} = \frac{M_y}{d_0} \tag{2}$$

where $M_y = W_{el} \cdot f_y$ is the bending yielding moment of the cross section (W_{el} is the elastic strength modulus of the cross-section).

The lateral force leading to the full plasticization of the knee cross-section F_{pl0} is given by:

$$F_{pl0} = \frac{M_{pl}}{d_0} \tag{3}$$

where $M_{pl} = f_y \cdot W_{pl}$ is the plastic bending moment of the cross section ($W_{pl} = \beta \cdot W_{el}$, β is the plastic benefit of the member cross-section).

By simple inspection of Eq. 1 and 2 it clearly appears that the lateral stiffness and the yielding force of a CSB can be set independently (within certain ranges) by properly defining the cross-section and the lever arm. On the contrary, traditional diagonal steel braces are characterized by a lateral stiffness which is coupled to the yielding force (they both basically depend upon the cross-section area).

The maximum tensile capacity of the CSB is reached for a lateral load *F* leading to the complete elongation of the CSB, i.e. when the lever arm *d* (and the angle θ) drop to zero. In this configuration, the device is uniquely subjected to axial load equal to the axial tensile capacity of the member:

$$N_{pl} = A \cdot f_y \tag{4}$$

In the work by Palermo et al. (2014) the idea of the “shock-absorbing soft-storey concept”, originally proposed at the end of 1960s by Fintel and Khan, was reviewed in the perspective of performance based seismic design with the purpose of proposing a “enhanced” first-storey “isolated” building. The seismic first-storey isolation is obtained through the insertion (only at the bottom level of the building) of CSBs, which are specifically designed in order to satisfy preselected seismic performance objectives. The objectives are identified through a target performances curve (e.g. a base shear - lateral displacement capacity curve) in terms of initial elastic behavior (lateral stiffness), first yielding, global ductility, and final hardening (to prevent excessive displacements due to P-Δ induced effects). The first interstorey drift represents the controlling parameter upon which the whole design procedure is grounded. After a very strong earthquake the magnitude of the residual deformation is limited thanks to the peculiar hardening behaviour of the devices (when they straighten up). The design approach was fully applied to the case of a five-storey steel frame building. The interested reader may find all additional details in the work by Palermo et al. (2014).

The main advantages in using CSBs as lateral resisting system with respect to other traditional (CBF) of advanced (BRB) systems relies in the uncoupling between the lateral stiffness and the yielding force due to their peculiar geometrical shape, as above mentioned.

The use of CSBs both as dissipative bracing systems placed along the whole building height and as beam-column hysteretic joint connections (Smith et al. 2014, Hsu and Halim 2017) are currently under investigation by the authors. For instance, possible placements are depicted in Figure 3.

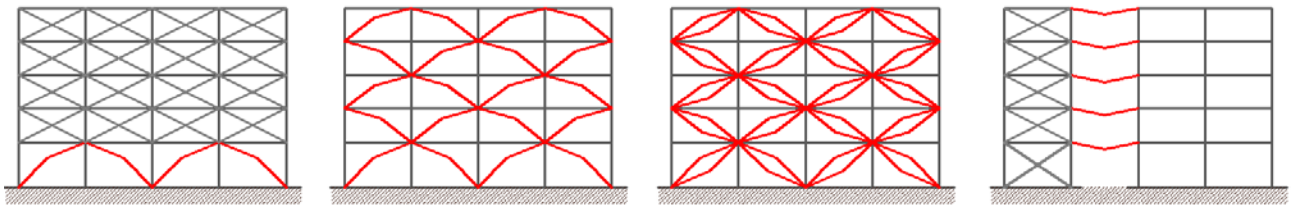

(a) *(b)* *(c)* *(d)*

Figure 3 – (a) First-storey CSB placement; (b) Inter-storey single CSB placement; (c) Inter-storey double CSB placement; (d) Coupling of adjacent structures with CSBs.

2.3 An equivalent 1-DOF mechanical system

Let us consider a bilinear symmetric CSB device as subjected to a horizontal force F (Figure 4a). Due to the geometrical shape of the CSB, the two straight members are subjected to a combination of bending moment and axial force (tension or compression depending on the sign of F). At first approximation, the CSB can be schematized as the 1-DOF mechanical system composed by two rigid members (of length L^*) connected at the knee point by a rotational spring of constant elastic stiffness $K_\theta = \dfrac{3 \cdot E \cdot J}{L^*}$ (Figure 4b). The spring is characterized by an elastic-perfectly plastic moment-rotation M-θ behavior.

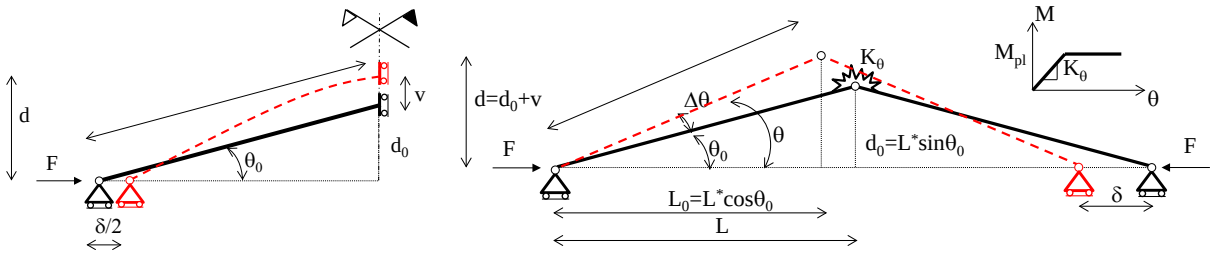

(a) (b)

Figure 4 – (a) One half of a bilinear symmetric CSB subjected to a lateral load F; (b) 1-DOF schematization of the bilinear symmetric CSB device subjected to a lateral load F.

The rotation $\Delta\theta$ is related to the lateral δ and vertical v displacements through the following trigonometric relationships:

$$\begin{aligned} \delta &= 2L^* \left(\cos\theta_0 - \cos\theta\right) \\ v &= L^* \left(\sin\theta - \sin\theta_0\right) \end{aligned} \tag{5}$$

Where $\theta = \theta_0 + \Delta\theta$ is the inclination of the diagonal member in the generic deformed configuration. The force displacement response of the 1-DOF system of Figure 4b is governed by the following set of equilibrium equations (Ballio and Mazzolani, 1996):

$$\begin{cases} F_e = K_L \cdot \delta & \text{for } \delta \le \delta_{y0} \\ F_{pl} = M_y \,/\left(d_0 + \dfrac{\delta}{2\tan\Delta\theta} \right) & \text{for } \delta > \delta_{y0} \end{cases} \tag{6}$$

$$K_L = K_\theta \cdot \frac{\Delta\theta}{2 \cdot L^{*2} \cdot \sin\theta\left(\cos\theta_0 - \cos\theta\right)} = \frac{3}{2} \cdot \frac{E \cdot J \cdot \Delta\theta}{L^{*3} \cdot \sin\theta\left(\cos\theta_0 - \cos\theta\right)} \tag{7}$$

where F_e and F_{pl} indicate the response within the elastic and plastic fields, respectively; $\delta_{y0} = \frac{2}{3} \cdot \frac{{d_0}^2}{\xi \cdot h \cdot \cos\theta_0} \cdot \varepsilon_y$ is the approximate yielding displacement, K_L is the lateral (flexural) stiffness of the system at the generic deformed configuration.

According to Eq. (6), for increasing absolute values of negative $\Delta\theta$ (i.e. increasing value of lateral force inducing tension in the diagonal members), after the first yielding in tension, the lateral force F would rapidly tend to infinite. Nonetheless, the maximum lateral force inducing tension in the member is limited by the material tensile strength, e.g. by the ultimate axial capacity of the straight member N_{pl} (Eq. 4). In this simple 1-DOF mechanical model the axial deformability has been neglected with respect to the flexural one.

The lateral displacement δ_{Npl} leading to $\theta = 0$ then can be estimated according to:

$$\delta_{Npl} = 2 \cdot (L^* - L_0) + 2 \cdot \varepsilon_y \cdot L^* + \Delta_{pl} \cdot \left(\varepsilon_u - \varepsilon_y\right) \tag{8}$$

where Δ_{pl} is equal to the length of the plastic hinge (Tremblay, 2002) and ε_u is the ultimate material strain. Note that in Eq. (8) the contribution of the axial deformability has been necessarily taken into account, since the configuration described by $\theta = 0$ is characterized by axial force only.

The set of simple equations from Eq. (1) to Eq. (8) allows to analytically capture the essence of the global force-displacement response of the single CSB. In order to assess the effectiveness of the above derived equations in capturing the actual force-displacement envelope response of a CSB device, numerical simulations using the non-linear Finite Element (FE) based software SeismoStruct (Pinho and Antoniou 2009) have been carried out. The fiber-based beam elements implemented in this software account for distributed inelasticity through integration of material response over the cross-section and integration of the section response along the length of the element. The use of fiber-based beam elements does not allow to consider (1) local/distortional buckling and (2) fatigue. However, from a practical design point of view: (1) local buckling may be overcome by the use of compact (namely Class 1 or 2) cross-sections (Uriz et al. 2008); and (2) fatigue issues are of secondary importance since the devices are designed as structural fuses that should be replaced after a strong earthquake. The study of these specific issues would require more sophisticated models (such as shell or solid FE models) and is out of the scope of the present work. Note that

also other studies related to experimental response of diagonal steel bracings used the fiber approach to model the elements (see Hsiao et al. 2012, 2013; D'Aniello et al. 2013, Uriz et al. 2008).

As an illustrative example, the non-linear force-displacement response of two devices with length L_0= 7 m and full rectangular (28 cm x 10 cm) cross-section are displayed in Figure 5. The devices have different normalized lever arms equal to ξ =0.1 and 0.2. In particular, the following curves are displayed:

- The numerical force-displacement responses obtained through the research software SeismoStruct (Pinho and Antoniou 2009) accounting for both geometrical (co-rotational model) and material (Menegotto-Pinto law) non-linearities (solid black curves);
- The responses of the equivalent 1-DOF mechanical systems (solid red curves);
- The linear elastic-rigid-plastic ERP response (dotted blue curve) is made by a tri-linear piecewise curve in tension (governed first by Eqs. (2) and (3) up to the plasticization of the knee section, and then by Eqs. (4) and (8) up to the exploitation of the full plastic capacity) and a bilinear curve in compression (governed by Eqs. (2) and (3)).

Clearly, the response of the 1-DOF system is quite approximated given that: (i) the plasticity is lumped in the knee section and (ii) the axial deformability is neglected. Nonetheless, the 1-DOF mechanical system (red dotted curve) is able to qualitatively capture the essence of the non-linear behavior of CSBs (black curve). In more detail:

- Under tension loading, the post-yielding branch of the 1-DOF mechanical system is stiffer than the numerical response given that the axial deformability has been neglected. Clearly, such contribution becomes more and more significant as the angle θ tends to reduce. When the angle θ is equal to zero, the CSB is uniquely subjected to axial force and therefore only the axial deformability governs its mechanical behavior.
- Under compression loading, the response is merely governed by the geometrical effects which are well captured by the simple 1-DOF model.

By comparing Figures 5c and d, it can be noted that the ductility tends to increase as the normalized lever arm ξ increases. Similarly, by comparing Figures 5e and f, it appears that the strength reduction (softening) tends to reduce as the normalized lever arm ξ increases.

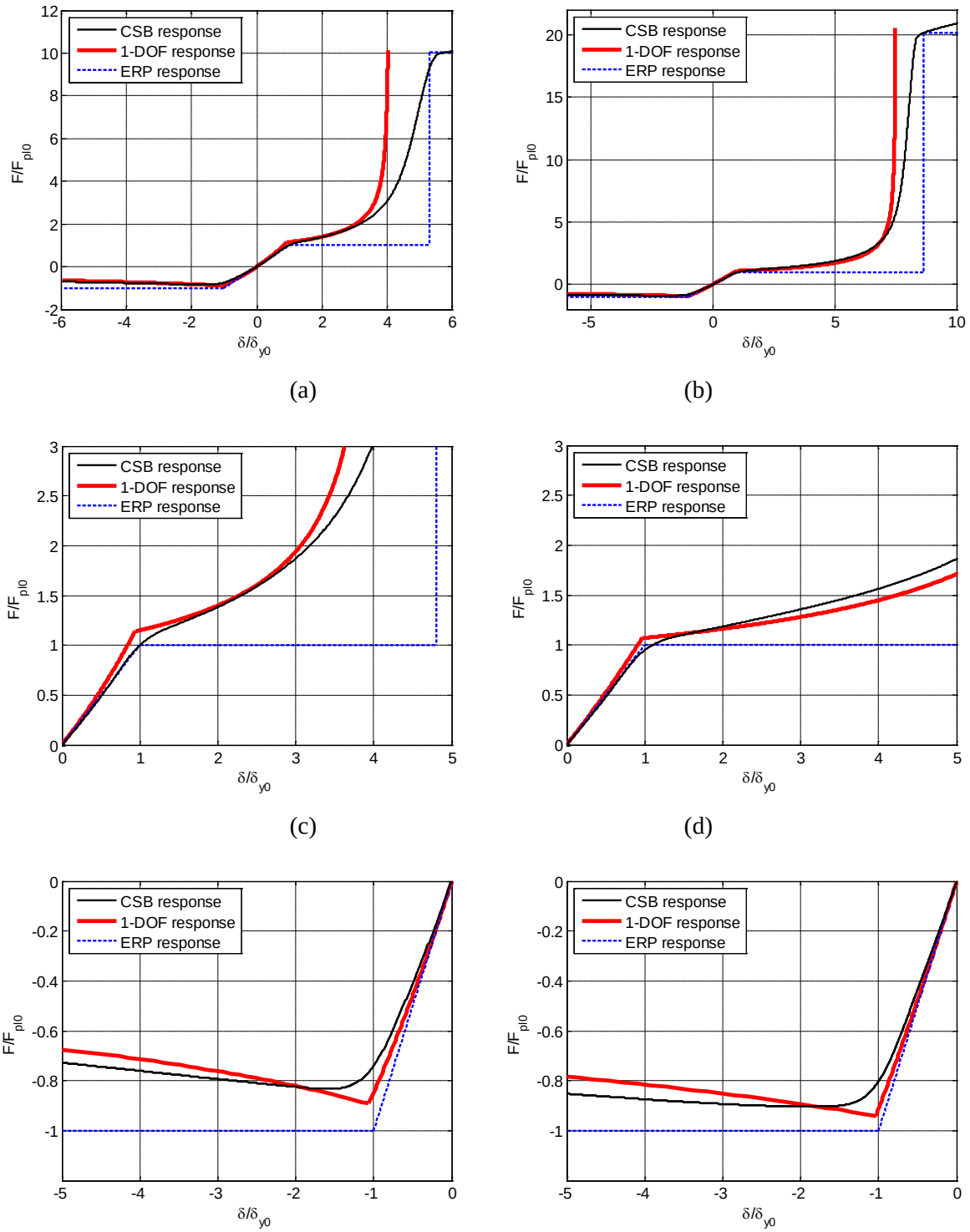

Figure 5 – The normalized force-displacement responses of the CSB device and of the 1-DOF mechanical system. (a) envelope (ξ=0.1); (b) envelope (ξ=0.2); (c) behavior in tension (ξ=0.1) (d) behavior in tension (ξ=0.2); (e) behavior in compression (ξ=0.1) (f) behavior in compression (ξ=0.2).

3. The experimental campaign

An experimental campaign has been carried out in 2014-2015 at the Structural Engineering and Geotechnical Laboratory (LISG) at the University of Bologna to assess the experimental non-linear cyclic behavior of scaled CSB steel specimens.

3.1 Geometrical and mechanical properties of the tested specimens

Nine scaled CSB specimens have been tested. All the specimens are characterized by a symmetric bilinear geometrical configuration with a normalized lever arm ξ=0.1 and scaling factors set to be representative of a device inserted in a frame having dimensions of 6 x 3 m (diagonal length of about 7 m) to be consistent with the numerical simulations developed in a previous work (Palermo et al. 2015). The two ends of the CSB present a connection plate with a central hole (nominal diameter of 32 mm) having the function of connecting the device to the testing machine. The specimens have been produced using different manufacturing processes: (i) laser-cutting a unique element from a flat steel plate of uniform thickness; (ii) welding together two straight segments at the knee section; (iii) welding two straight elements to the V-shaped knee element (three components in total); (ii) bending with a spindle an initial straight element having a length equal to the length of the two straight segments. In more details, the following cross-sections were utilized: (i) full rectangular (symbol R) with a height-to-width ratio equal to 3; (ii) full circular (symbol C); (iii) tubular circular (symbol T); (iv) full rectangular with a central stiffening ribs (symbol RR). Some specimens were tested under monotonic cyclic loadings (tension, T, or compression, C), while others were tested under cyclic reserved loadings (R). In one case, after imposing a cyclic loading history in compression the specimen has been subjected to a final monotonic loading in tension (C+T) up to the failure.

Structural steel S275JR (with nominal characteristic yielding stress $f_{yk} = 275\ MPa$ and characteristic ultimate stress $f_{uk} = 410 - 560\ MPa$, according to EN 10025-2 2004) has been used for all specimens. Tests on small steel specimens have been carried out to evaluate the actual material properties. The actual yield stress varied between 300 MPa and 400 MPa. Table 1 identifies all the tested specimens summarizing their main properties. For instance, R1-T indicates a full rectangular cross-section which has been tested under cyclic loadings in tension. Figure 6 and 7 provides photos and CAD drawings of all specimens.

Table 1: The main properties of the tested specimens.

			Geometrical properties				
Specimen	Manufacturing	Loading protocol	*h* [mm]	*A* [mm^2]	*J* [mm^4]	*L* [mm]	ξ [-]
R1-T	laser-cut	Tensile	41.4	621	8870	1040	0.10
R2-C	laser-cut	Compression	41.4	621	8870	1040	0.10
R3-R	laser-cut	Reversed	41.4	621	8870	1040	0.10
RR1-R	laser-cut with additional welded ribs	Reversed	41.4	770	8920	1040	0.10

RW1-C+T	welded at the middle of each straight segment	Reversed	41.4	621	8870	1040	0.10
C1-T	bent	Tensile	35.0	962	8990	980	0.10
C2-C	bent	Compression	35.0	962	8990	980	0.10
C3-R	bent	Reversed	35.0	962	8990	980	0.10
TW1-R	welded at the knee section	Reversed	42.0	333	6470	1060	0.10

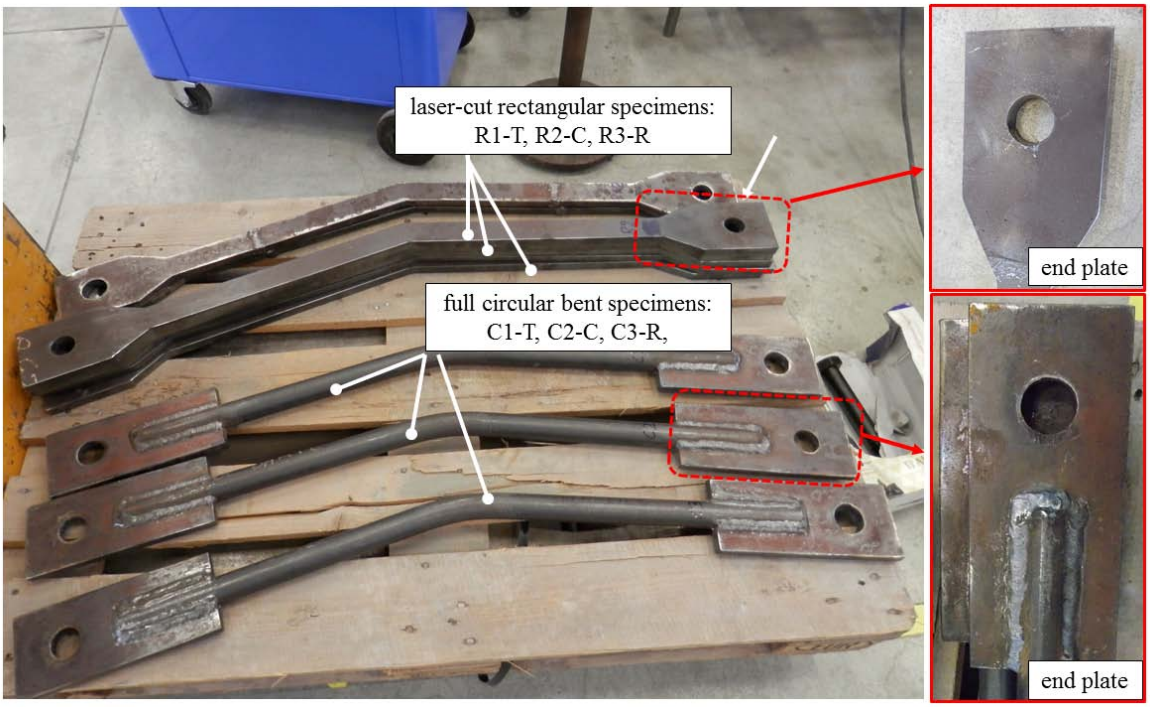

(a)

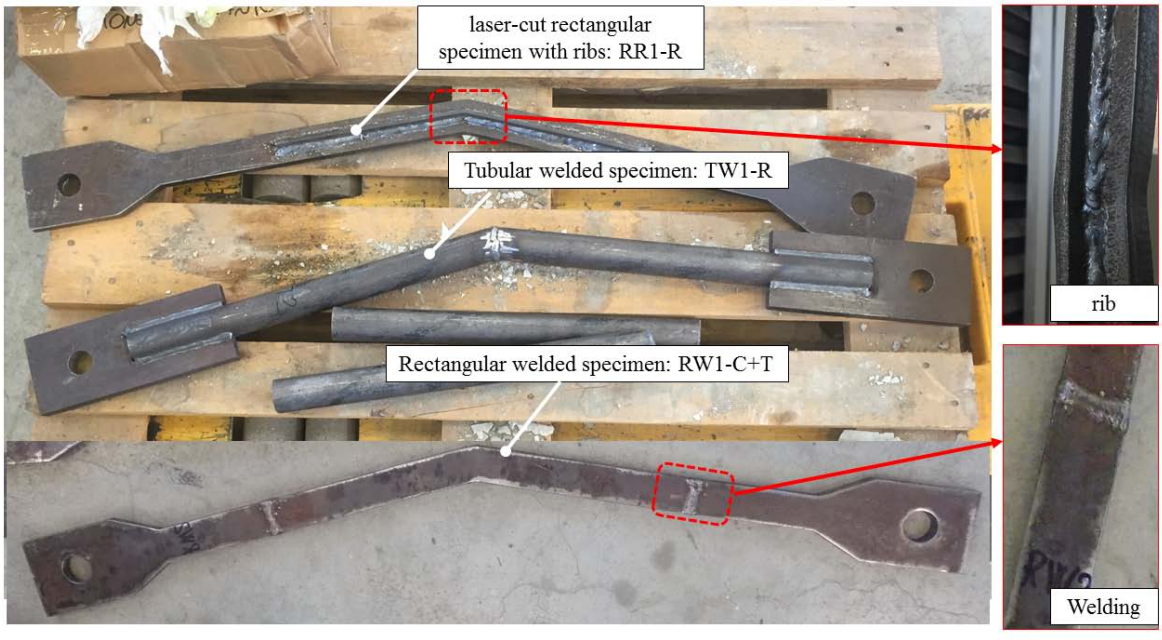

(b)

Figure 6 – Photos of the tested specimens: (a) R1-T, R2-C and R3-R; C1-T, C2-C and C3-R; (b) RW1-C+T, RR1-R and TW1-R.

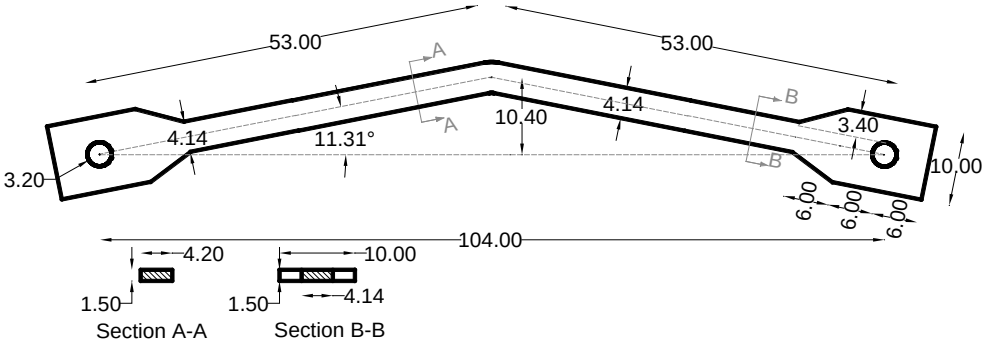

(a)

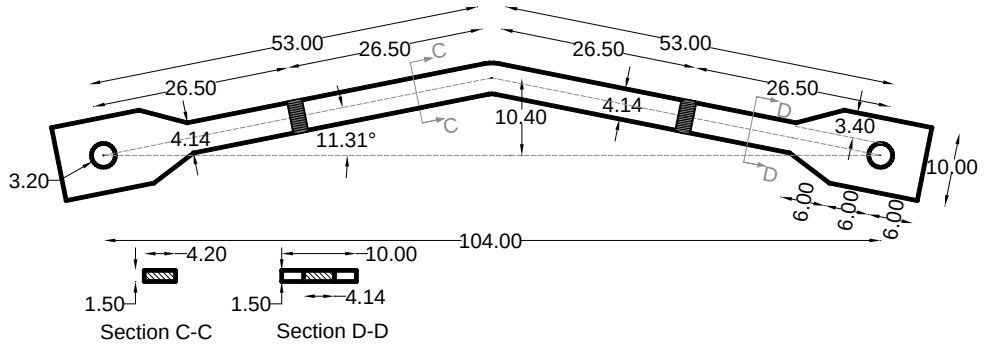

(b)

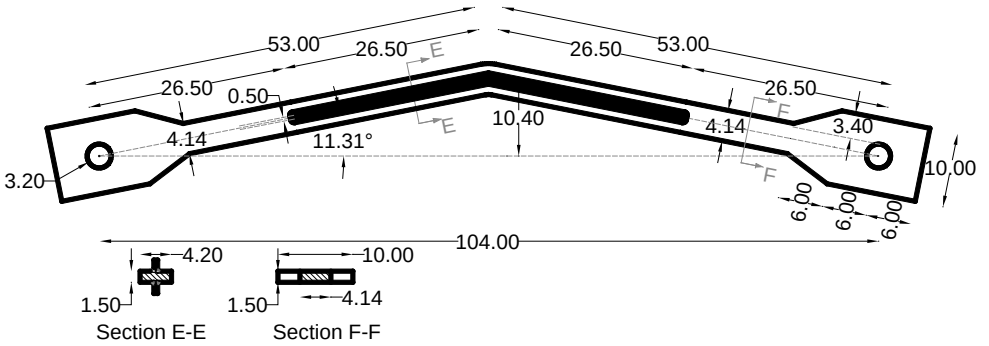

(c)

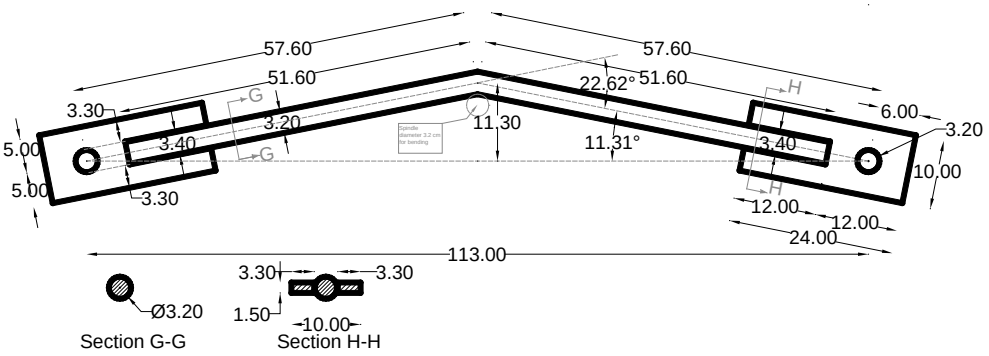

(d)

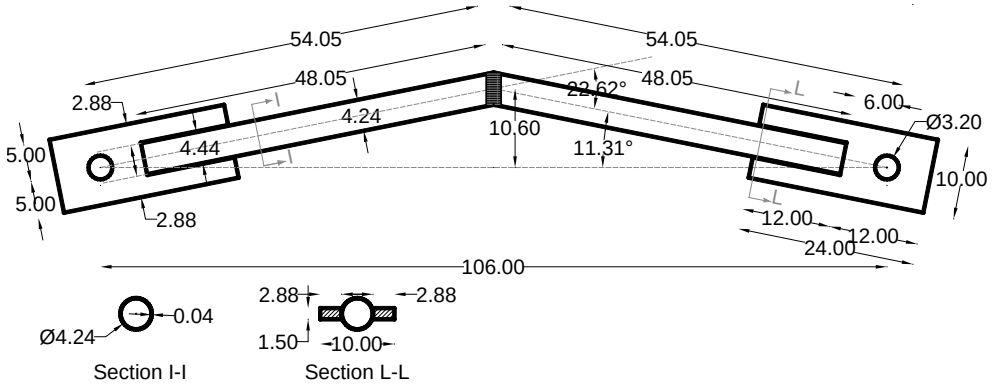

(e)

Figure 7 – The geometrical configuration of the tested specimens (dimensions are in cm units): (a) specimens with full rectangular cross-section (R); (b) welded specimens with full rectangular cross-section (RW); (c) specimens with full rectangular cross-section and ribs (RR); (d) specimens with full circular cross-section (C); (e) welded specimen with tubular cross-section (TW)

3.2 Test setup and loading protocols

The monotonic and reversed cyclic pseudo-static tests were performed using a universal METRO COM machine with a nominal capacity of 600 kN (Figure 8). The specimen is inserted between two U-shaped box connectors (whose axis is aligned along the vertical direction) through Ø30 mm high strength bolts, so that rotations are permitted (pinned connections). The loads/displacements are applied to the top U-shaped box by mean of a hydraulic actuator (displacement increments of 2 *mm/min* – 5 *mm/min*). The instrumentation is supplemented by a system of acquisition and data post processing.

(a) (b)

Figure 8 – (a) METROCOM material testing machine; (b) Test setup

The Digital Image Correlation (DIC) technique is used to monitor the surface deformation field. The monitoring is performed using a VIC-3D HR system, with a hardware composed by two cameras with a resolution of 14 Megapixel (in terms of deformation the resolution is around 50 $\mu\varepsilon$). In order to use the DIC technique, the surface of the specimen is treated with white painting and black dots.

The typical loading protocols used for the monotonic tests and reversed cyclic is summarized in Table 2 in terms of maximum imposed displacement δ_{max} (absolute value) at each cycle as normalized with respect to the first yielding displacement δ_y. Clearly, the actual imposed loading histories could vary slightly from one specimen to another. All the applied loading histories are displacement controlled. The amplitudes of the first cycles are set in order to investigate the initial elastic behavior, and then they progressively increase up to large amplitudes (> 8 δ_y) or failure.

Table 2: Nominal Loading protocol.

Number of cycles	δ_{max}/δ_y
4	0.25
4	0.50
4	1.00
3	2.00
3	4.00
3	8.00
1	failure

3.3 The main goals

The main objective of the experimental campaign is to provide a complete experimental assessment of the pseudo-static cyclic response of CSB devices and to verify the effectiveness of the design formulations. To achieve the objective, the following specific aspects are discussed in the following sections:

- An overview of the experimental force-displacement response (section 4.1);
- The comparison between the experimental responses and the prediction provided by the analytical formulas of section 2 (section 4.2);
- The comparison between the theoretical force-displacement response of the equivalent 1-DOF mechanical model and the envelope of the experimental response (section 4.3);
- The assessment of the ductility capacity (section 5);
- To assessment of the non-linear cyclic response in terms of energy dissipation capacity (section 6);
- The influence of the different manufacturing processes on the failures under different loading protocols (section 7);
- The monitoring of the local deformation fields through the DIC technique (section 8).

4. The experimental force-displacement response

4.1 The unprocessed force-displacement responses

The unprocessed experimental force-displacement responses of all specimens are shown in Figure 9. The recorded responses include the small displacements due to the slacks related to the oversized holes. The two rectangular R1-T and R2-C specimens and the two circular C1-T and C2-C specimens exhibited a stable in-plane cyclic behavior under monotonic tensile and compressive loads. On the contrary, the rectangular R3-R specimen buckled out-of-plane when subjected to cyclic loadings in compression after yielding in tension due to the unfavorable height-to-width ratio (around 3) of the cross-section leading to a very low out-of-plane moment of inertia ($J/I = 9$). The circular C3-R specimen (characterized by equal in-plane and out-of-plane cross-section moment of inertia) did not buckle out-of-plane. Similarly, the rectangular RR1-R, did not show a significant out-of-plane response, thanks to the presence of the ribs leading to an increase in the out-of-plane cross section moment of inertia. The rectangular welded RW1-C+T showed a stable cyclic in-plane behavior under the initial cycles in compression and also during the subsequent cycles in tension up to the end of the test. The tubular welded TW1-R showed a not stable cyclic behavior with a progressive degradation of the tensile strength.

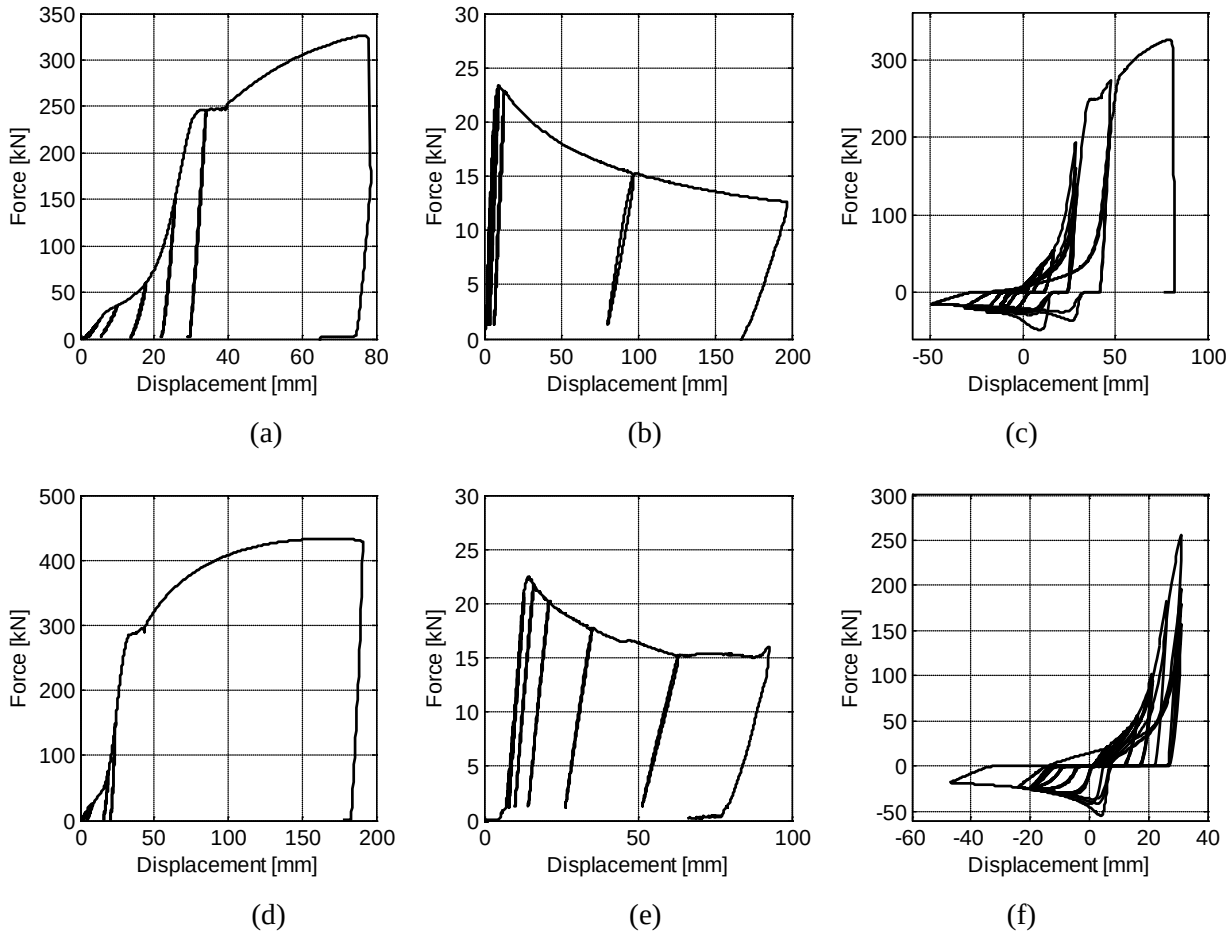

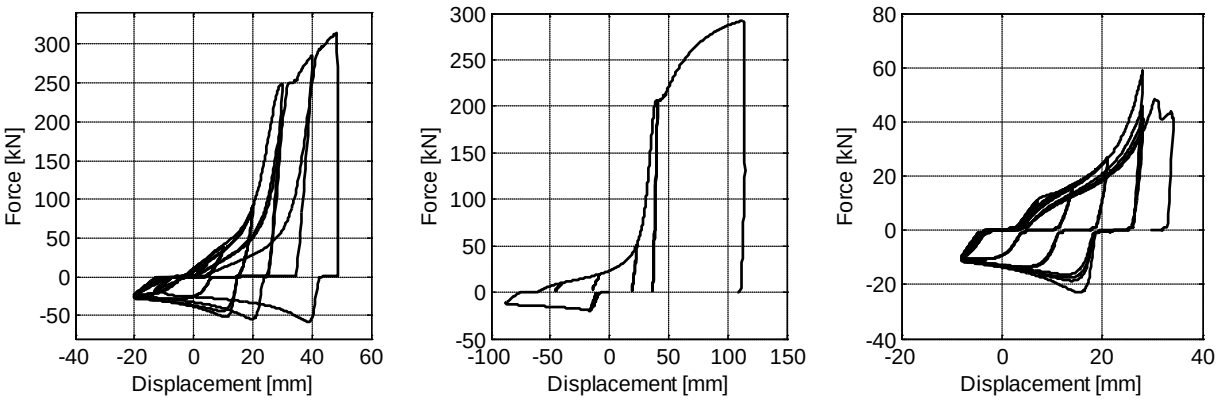

(g) (h) (i)

Figure 9 – Experimental force-displacement cyclic response for specimen (a) R1-T; (b) R2-C; (c) R3-R; (d) C1-T; (e) C2-C; (f) C3-R; (g) RR1-R; (h) RW1-C+T; (i) TW1-R.

4.2 Initial lateral stiffness, first yielding force and maximum lateral force

The values of the initial lateral stiffness K_{L0}, the lateral forces leading to the first yielding F_y and the maximum absolute value of the recorded forces F_{peak} obtained from the experimental tests are reported in Table 3 and compared with the predictions as given by Eqs. (1) - (4). The values of the experimental force leading to the first yielding F_y are obtained from visual inspection of the recorded force-displacement response.

Table 3: Initial lateral stiffness, first yielding force and maximum absolute value of the lateral force.

	K_{L0} [kN/mm]		F_y [kN]		F_{peak} [kN]		
Specimen	Experimental	Eq. 1	Experimental	Eq. 2	Experimental	Eq. 3 (C)	Eq. 4 (T)
R1-T	4.2	4.8	17	15.5	324	23.2	248
R2-C	4.0	4.8	16	15.5	22	23.2	248
R3-R	3.4(C) ÷ 4(T)	4.8	10(C) ÷ 15(T)	15.5	22(C) ÷ 320(T)	23.2	248
RR1-R	4.1(C) ÷ 6(T)	4.9	15(C) ÷ 20(T)	15.7	57(C) ÷ 300(T)	23.6	308
RW1-C+T	3.6 (C)	4.8	15 (C)	15.5	18(C) ÷ 290(T)	23.2	248
C1-T	3.9	4.7	18	16.3	420	27.7	385
C2-C	3	4.7	15	16.3	21.3	27.7	385
C3-R	3.3(C) ÷4.7(T)	4.7	10(C) ÷ 11(T)	16.3	54(C) ÷ 250*(T)	27.7	385
TW1-R	2.7(C) ÷2.7(T)	3.4	6(C) ÷ 8(T)	10.7	22(C) ÷ 58(T)	14.4	133

(C) refers to the behavior in compression; (T) refers to the behavior in tension; (*) the test was stopped at the first signs of ovalization of the holes (see also section 7).

4.3 Experimental Envelopes vs 1-DOF analytical responses and numerical responses

The envelope of experimental force-displacement responses (in tension and compression) of the full rectangular and full circular specimens (i.e. R1-T, R2-C and C1-T, C2-C) are shown in Figure 10 (thick – black line) and compared with the numerical response (thin-black line) and the analytical response of the 1-

DOF mechanical system (red line) as described in section 2.3. The ERP response is displayed in blue thin dotted lines. In the numerical simulations (SeismoStruct software), the steel material is characterized by an elastic modulus E= 200000 MPa; a yield stress f_y calibrated on the of material test results, an hardening ratio r=0.5%.

In tension, up to a lateral displacement of 15 mm, both the analytical response of the 1-DOF mechanical system and the numerical response are practically coincident with the experimental envelopes. As already highlighted in section 2.3, for large displacements under tensile loadings the response of the 1-DOF system becomes stiffer given that the axial flexibility has been neglected; the numerical response is still slightly stiffer than the experimental envelopes. In compression, both the analytical 1-DOF response and the numerical response are able to accurately capture the experimental envelopes. The ERP response is displayed considering $\Delta_{pl} = 0.05 \cdot L^*$ and $\varepsilon_u = 10\%$.

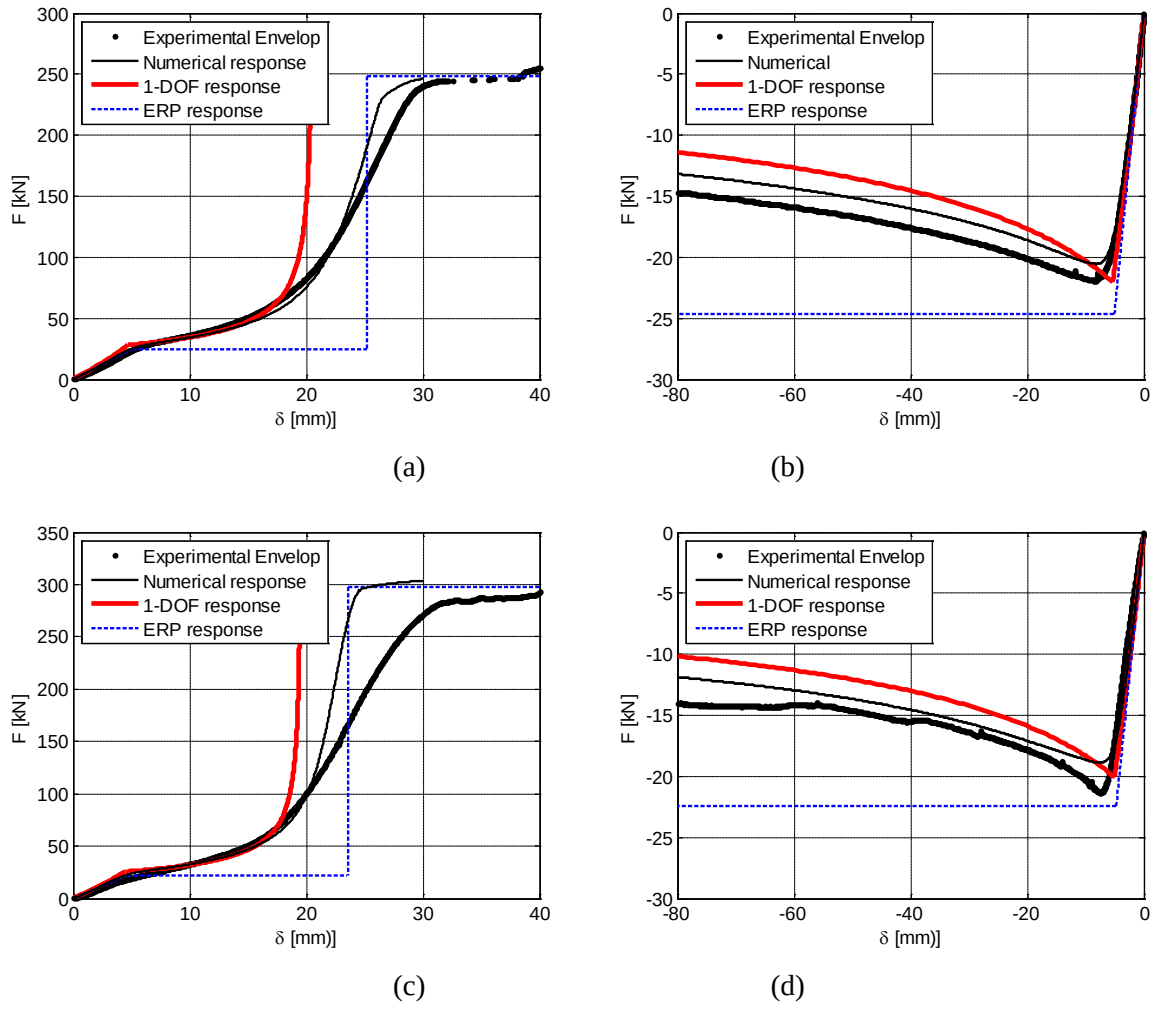

Figure 10 – Experimental envelop vs analytical and numerical response: (a) R1-T; (b) R2-C; (c) C1-T; (d) C2-C.

5. Ductility capacity

The displacement ductility capacity of the CSB is here evaluated with respect to the condition of the first yielding at the knee section by considering the response of the equivalent bilinear system characterized by

equal area (i.e. dissipated energy) under the force-displacement response. The stiffness of the equivalent bilinear system is given by Eq. (1). For instance, Figure 11 displays the normalized force-displacement response of the full rectangular and full circular specimens in terms of normalized force (F/F_y^*) vs displacement ductility μ. Values of F_y^* have been obtained from the experimental responses by imposing equal areas under the experimental envelope (black solid lines) and the idealized bilinear responses (red dotted lines).

In tension the ductility capacity is limited (values around 2) and depends mainly on the specific geometry of the CSB (lever arm and cross-section) rather than the material ductility, as also noted in section 2.3. However, as above mentioned, it has to be remarked that the ductility under tensile loadings is here evaluated with respect to the first yielding force which is quite less (even 10 times) with respect to the ultimate tensile capacity of the device. At ultimate conditions under tensile loadings the CSB behaves as a conventional steel member subjected to a tensile axial load whose ultimate ductility capacity is mainly governed by the material ductility (stress-strain material behavior). In compression CSBs exhibit larger values of ductility capacity (around 5).

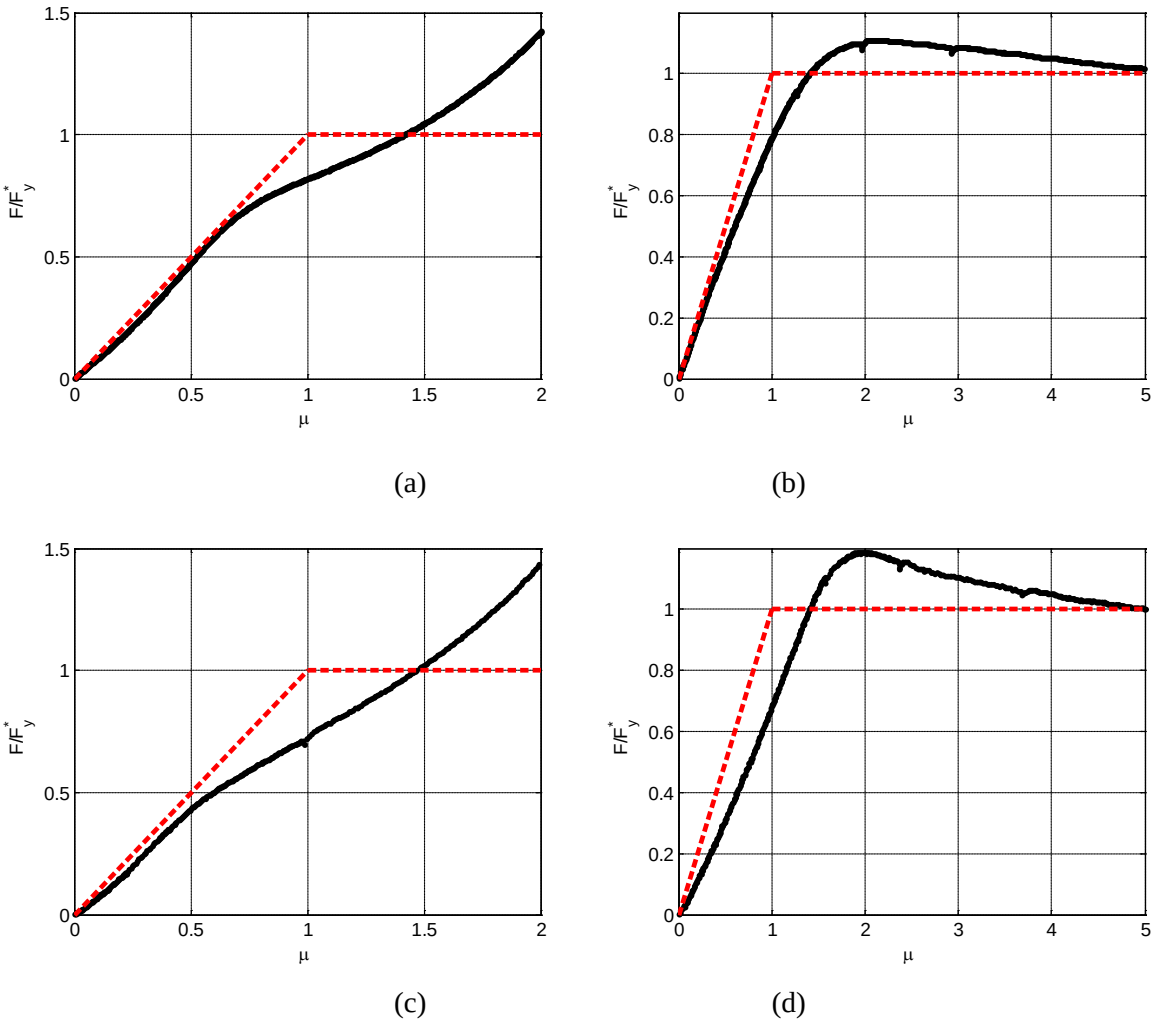

Figure 11 – Normalized response to evaluate the ductility capacity: (a) R1-T; (b) R2-C; (c) C1-T; (d) C2-C.

6. Cyclic energy dissipation capacity

The energy dissipation capacity of the CSB is here evaluated by means of the equivalent damping ratio $\zeta_{eq,i}$ according to Jacobsen (1930), referring to the *i-th* half hysteresis cycle:

$$\zeta_{eq,i} = \frac{1}{\pi} \cdot \frac{A_{half,i}}{F_{\max,i} \cdot \delta_{\max,i}} \tag{9}$$

where $A_{half,i}$ is the energy dissipated by the CSB in the *i-th* half hysteresis cycle; $F_{\max,i}$ and $\delta_{\max,i}$ are the maximum recorded force and displacement in the *i-th* half cycle, respectively. Figure 12 shows the average values (along the cycles at the same imposed displacement) of the equivalent damping ratio as resulted from tests R3-R and C3-R. The values of the equivalent damping ratios obtained from the half cycles in tension and the half cycles in compression are indicated with ζ_{eq}^{+} and ζ_{eq}^{-}, respectively.

As expected, due the asymmetric behavior in tension and compression, the CSBs exhibit quite different dissipative capacities when subjected to cyclic loadings in compression or tension: ζ_{eq}^{-} maximum values are around 0.22, while ζ_{eq}^{+} maximum values remain below 0.15.

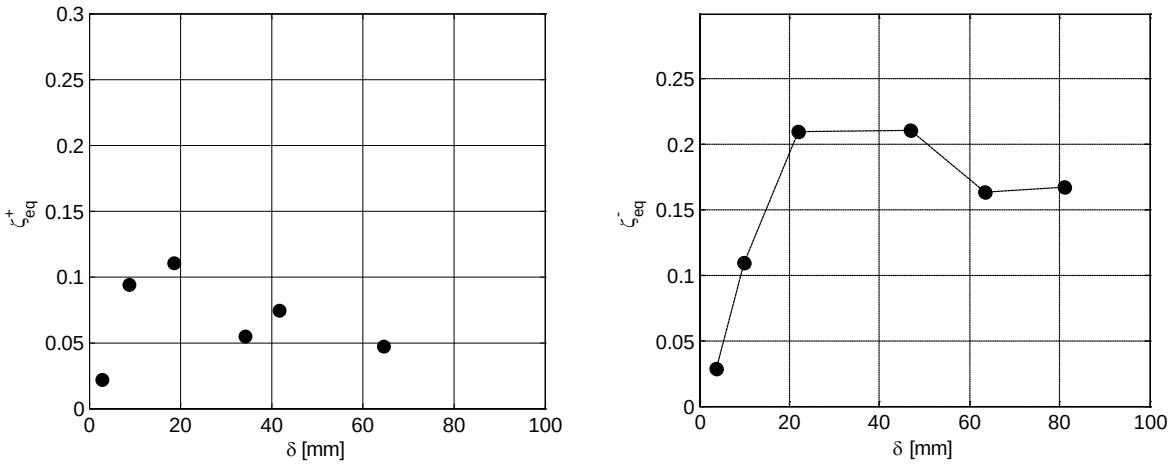

(a) (b)

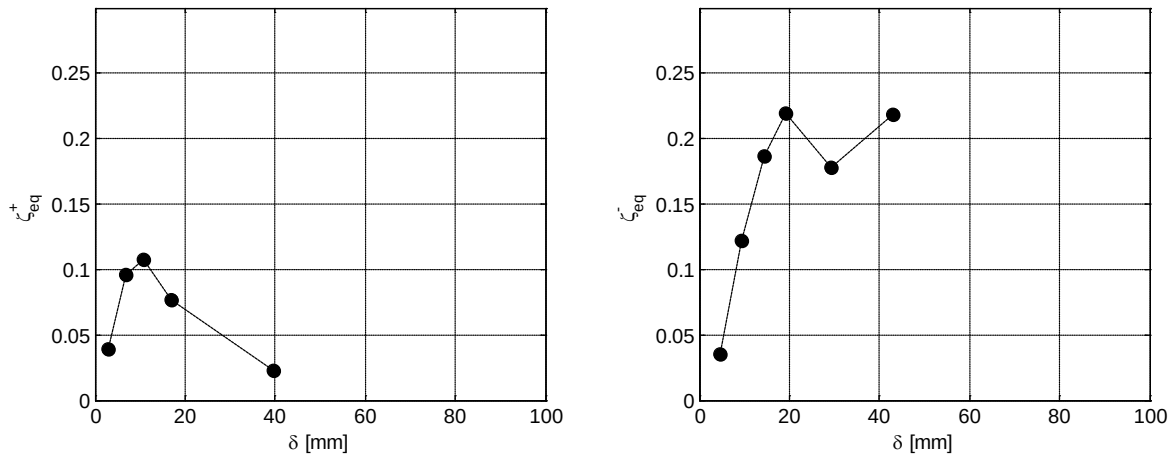

(c) (d)

Figure 12 – Equivalent damping ratios for specimens: (a) R3-R in tension; (b) R3-R in compression; (c) C3-R in tension; (d) C3-R in compression.

The values of the energy dissipation capacity under tensile loadings are limited. In compression a good dissipative response is obtained, even though the softening response does not allow to exploit the "full plastic dissipation capacity" (i.e. the dissipation capacity of an elastic-perfectly plastic device). From a practical point of view, the overall dissipation capacity could be enhanced by adopting the symmetric disposition (see Figure 1b). Experimental cyclic tests on this CSBs configuration will be the next step of the research.

7. Ultimate behavior

The relevant indication at ultimate behavior are summarized in Table 4. Photos of selected specimens showing a relevant step during the test (e.g. incipient failure in tension, large in-plane deformations, out-of-plane buckling) are collected in Figure 13. Not all the specimens were tested up to the failure due to limitations of the testing machine (during some tests too severe holes ovalizations of the connecting bolts has been observed and the tests were stopped).

Table 4: Observed failures/ultimate behavior

Specimen	Failure in tension	Out-of-plane buckling	Notes
R1-T	YES	/	Failure at the knee section
R2-C	/	NO	
R3-R	YES	YES	Failure at the knee section
C1-T	NO	/	Significant plastic ovalization of the holes
C2-C	NO	NO	
C3-R	NO	NO	Significant plastic ovalization of the holes
RR1-R	NO	NO	Significant plastic ovalization of the holes
RW1-C+T	YES	NO	Failure at the knee section
TW1-R	YES	NO	Significant strength degradation with final failure at the knee section

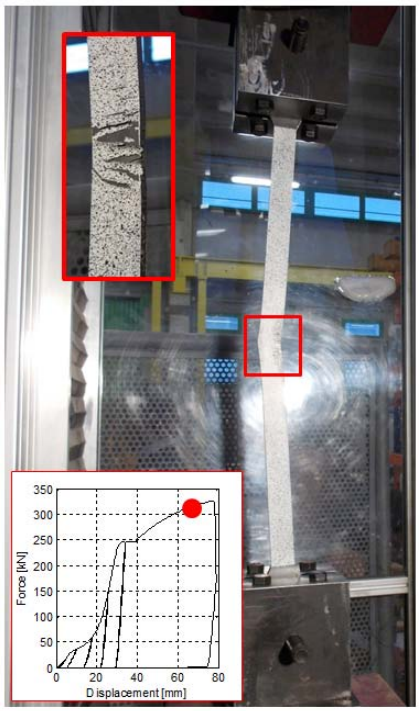
Force [kN]
Displacement [mm]

(a)

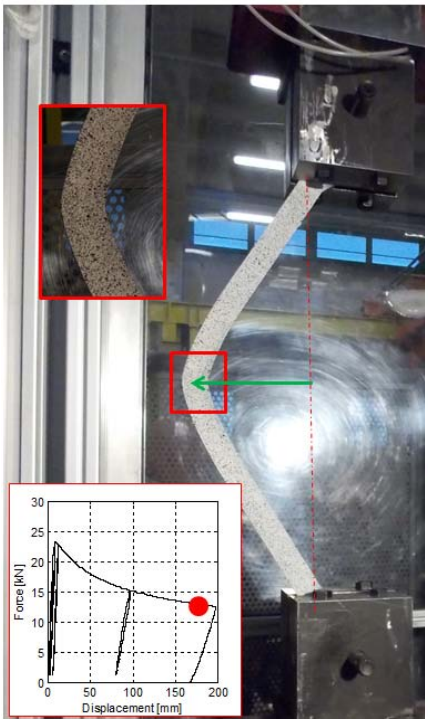
Force [kN]
Displacement [mm]

(b)

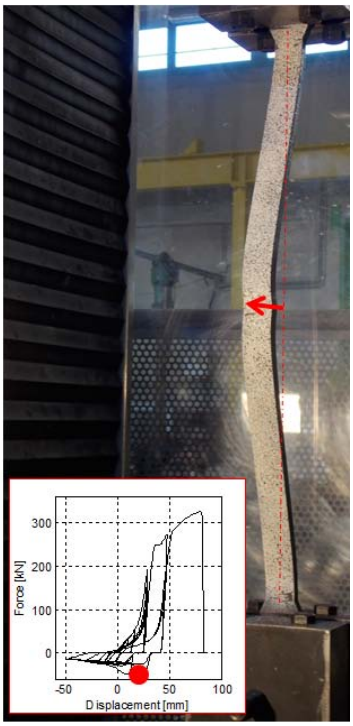
Force [kN]
Displacement [mm]

(c)

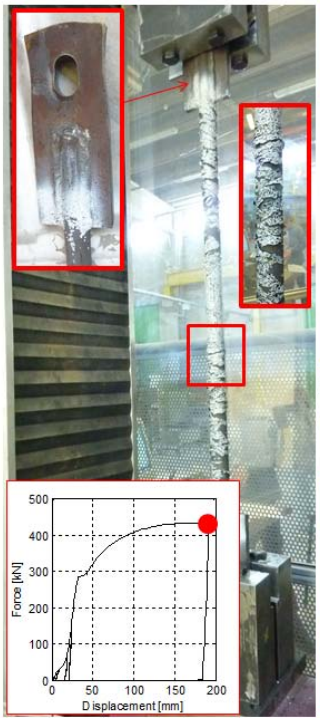
Force [kN]
Displacement [mm]

(d)

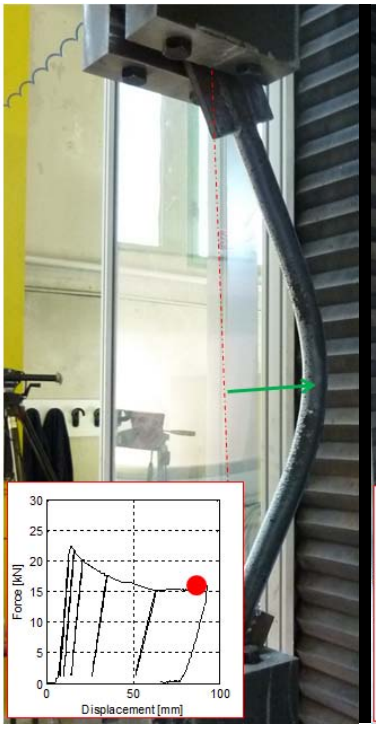
Force [kN]
Displacement [mm]

(e)


Force [kN]
Displacement [mm]

(f)

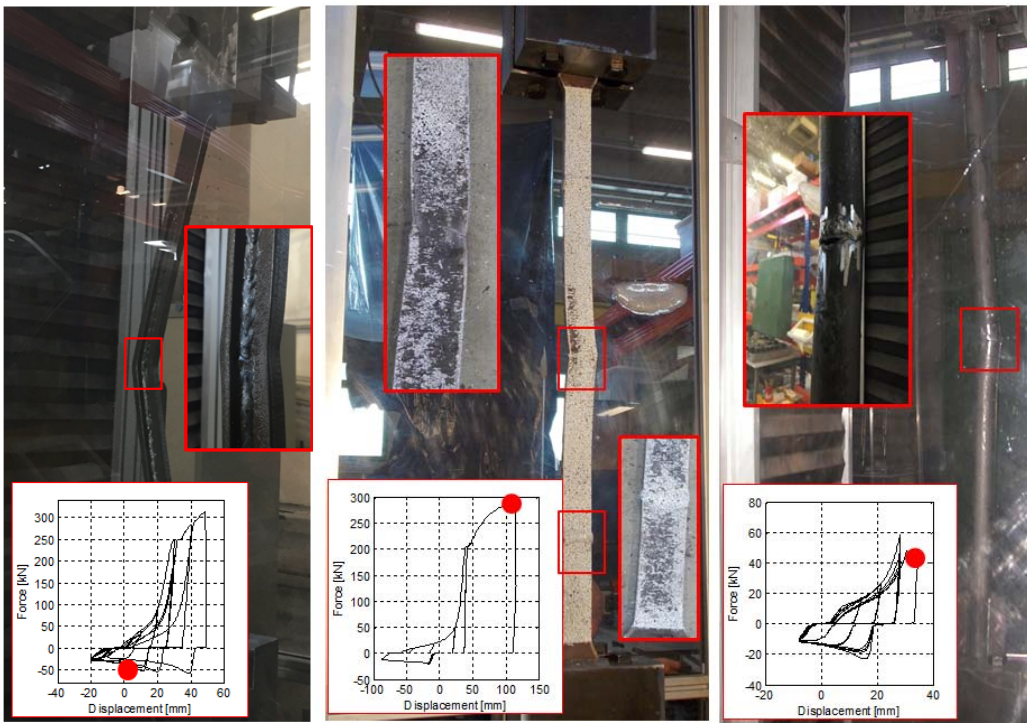

(g) (h) (i)

Figure 13 – (a) Failure in tension, specimen R1-T; (b) in-plane response under compression, specimen R2-C; (c) out-of-plane buckling, specimen R3-R; (d) failure in tension, specimen C1-T; (e) in-plane response under compression, specimen C2-C; (f) in-plane response under compression, specimen C3-R; (g) in-plane response in compression, specimen RR1-R; (h) failure in tension, specimen RW1-C+T; (i) failure in tension, specimen TW1-R.

The failure due to achievement of the ultimate tensile strain at the knee section of specimen R1-T is shown in Figure 13a. The in-plane deformed configuration of specimen R2-C is shown in Figure 13b. The out-of plane response (buckling) of R3-R when subjected to cyclic compression after yielding in tension is represented in Figure 13c. The deformed configuration under tensile loads of specimen C1-T is shown in Figure 13d. It can be noted that an important plastic deformation of the holes was observed during the tests which prevented to increase the load up to the final failure of the specimen in tension. No evidences of out-of-plane response were detected for the circular specimens C2-C and C3-R even after yielding in tension (Figure 13e, f). Similarly, the rectangular RR1-R, thanks to the presence of the ribs, did not show a significant out-of-plane response. The significant ovalization of the holes did not allow increasing the loads up to the final failure of the specimen in tension. However, even at large tensile loads (> 300 kN) the welding did not show any significant sign of degradation (Figure 13g). The welding of RW1-C+T did not show a visible degradation up to the final failure in tension of the specimen at the knee section (Figure 13h). The tubular welded TW1-R, due to a premature degradation of the welding at the knee, failed at a value of lateral force well below its theoretical strength (Figure 13i).

8. Deformation fields

Deformation fields have been obtained through the DIC technique. For selected tests, Figure 14 displays the strain contour maps corresponding to relevant point of the force-displacement response (identified by gray dots in the force displacement-response diagram).

The strain field within the elastic range is shown in Figure 14a for the full rectangular specimen R2-C subjected to a negative lateral force. As expected, the maximum strains are concentrated at the top and bottom of the knee region.

The deformation field of specimen C1-T within the plastic range (well beyond the first yielding) under a positive lateral force is displayed in Figure 14b. The deformation field corresponding to point 1 of the force-displacement response (the configuration at which the device is completely elongated), allows to appreciate the extension of the plastic zone. From a simple visual inspection, it appears around 1/3 of the length of the specimen. The deformation fields representative of point 2 and 3 of the force-displacement response allow to capture the evolution of plastic deformations up to the rupture.

Finally, Figure 14c shows the deformation fields within the plastic range under a negative lateral force for specimen C2-C. It can be noted that the deformation field remains quite uniform even up to an imposed lateral displacement of 10 cm corresponding to an increase of 100% in the lever arm.

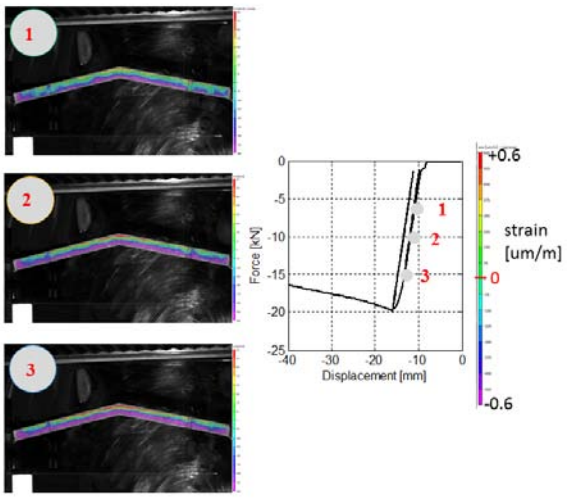

(a)

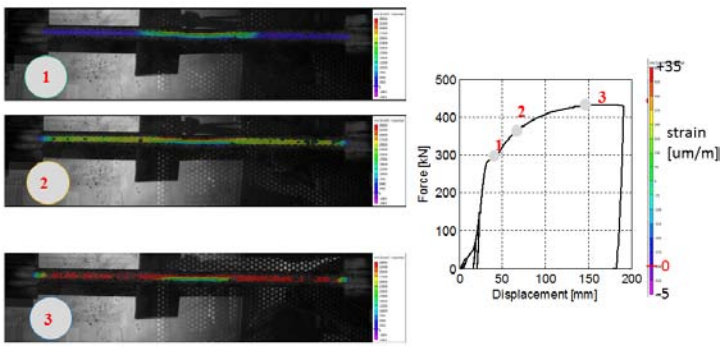

(b)

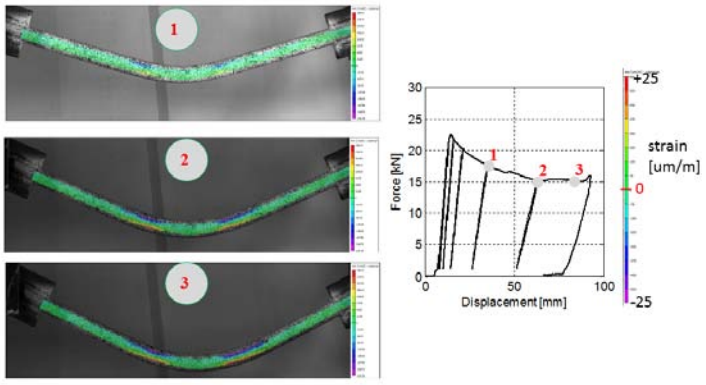

(c)

Figure 14 – Deformation fields as recorded by the DIC technique at relevant points of the force-displacement response: (a) RW1-T; (b) C1-T; (c) C2-C.

9. Conclusions

The paper presents the results of the first experimental campaign devoted to assess the nonlinear cyclic behavior of a novel steel hysteretic bracing device, known as Crescent Shaped Brace (CSB). Previous studies indicated that, from a theoretical point of view, the device, thanks to its geometrical shape, has a number of desirable seismic properties, such as the initial lateral stiffness uncoupled from the first yield strength, a significant ductile capacity and a final hardening to prevent from P-Δ induced collapses.

First, the experimental findings confirm the expected theoretical behavior of the device, thus suggesting that CSBs could be efficiently used as an enhanced alternative to the conventional steel diagonal concentric brace or the more advanced buckling resisting braces and scorpion devices. In addition, the main results of the experimental campaign may be summarized as follows:

- the rectangular profiles with a large height-to-width ratio tend to experience significant out-of-plane buckling after exposed to large elongations in tension. Such effect is prevented by using cross sections with larger out-of-plane moment of inertia (such as the circular and the rectangular with ribs cross sections);
- CSB made by two straight members welded at the knee cross-section experienced a sudden premature fragile failure at the knee section. Thus, when it is not possible to obtain a device from a unique element (e.g. laser-cut manufactured), the welding should be realized far from the knee sections and from the ends of the members.

Future experimental tests in order to complete the experimental assessment of different CSBs dispositions will be carried out to exploit the overall non-linear behavior of different CSB dispositions.

10. Acknowledgements

Financial supports of Department of Civil Protection (DPC-Reluis 2014–2018 Grant—Research line 6: ‘‘Seismic isolation and dissipation’’) is gratefully acknowledged. The authors would like to thank Benedetta Ferri and Raffaele Arena for their contributions in the execution of the experimental tests and preliminary interpretation of the experimental results.

References

Ballio, G., & Mazzolani, F. M. (1996). Strutture in acciaio: sistemi strutturali, sicurezza e carichi, materiale, unioni e collegamenti, resistenza e stabilità. Ulrico Hoepli.

Black, C. J., Makris, N., & Aiken, I. D. (2004). Component testing, seismic evaluation and characterization of buckling-restrained braces. Journal of Structural Engineering, 130(6), 880-894.

Christopoulos, C., Filiatrault, A., & Bertero, V. V. (2006). Principles of passive supplemental damping and seismic isolation. Iuss press.

D’Aniello, M., La Manna Ambrosino, G., Portioli, F., Landolfo, R. (2013). Modelling aspects of the seismic response of steel concentric braced frames. Steel and Composite Structures, An International Journal, 15(5), 539-66.

Di Cesare, A., Ponzo, F. C., Nigro, D., Dolce, M., & Moroni, C. (2012). Experimental and numerical behaviour of hysteretic and visco-recentring energy dissipating bracing systems. Bulletin of Earthquake Engineering, 1-23.

EN, C. (2004). 10025–2: Hot rolled products of structural steels–Part 2: Technical delivery conditions for non-alloy structural steels. *Brussels, Belgium: European Committee for Standardisation*.

Fintel, M., & Khan, F. R. (1968). Shock-Absorbing Soft Story Concept for Multistory Earthquake Structures. Portland Cement.

Gray, M. G., Christopoulos, C., & Packer, J. A. (2010, July). Cast steel yielding fuse for concentrically braced frames. In Proceedings of the 9th US National and 10th Canadian Conference on Earthquake Engineering (Vol. 9). Oakland, CA, USA and Ottawa, ON, Canada: Earthquake Engineering Research Institute and the Canadian Association for Earthquake Engineering.

Gray, M. G., Christopoulos, C., Packer, J. A., & Lignos, D. G. (2014). Development, Validation and Modeling of the new Cast Steel Yielding Brace System. In Proceedings of Structures Congress 2012 (pp. 71-82).

Hsiao, P. C., Lehman, D. E., & Roeder, C. W. (2012). Improved analytical model for special concentrically braced frames. Journal of Constructional Steel Research, 73, 80-94.

Hsiao, P. C., Lehman, D. E., & Roeder, C. W. (2013). A model to simulate special concentrically braced frames beyond brace fracture. Earthquake engineering & structural dynamics, 42(2), 183-200.

Hsu, H. L., & Halim, H. (2017). Improving seismic performance of framed structures with steel curved dampers. Engineering Structures, 130, 99-111.

Palermo, M., Ricci, I., Gagliardi, S., Silvestri, S., Trombetti, T., & Gasparini, G. (2014). Multi-performance seismic design through an enhanced first-storey isolation system. Engineering structures, 59, 495-506.

Palermo, M., Silvestri, S., Gasparini, G., & Trombetti, T. (2015). Crescent shaped braces for the seismic design of building structures. Materials and Structures, 48(5), 1485-1502.

Pinho, R., & Antoniou, S. (2009). SeismoStruct Computer Program.

Robinson, W., & Greenbank, L. (1976). An extrusion energy absorber suitable for the protection of structures during an earthquake. Earthquake Engineering & Structural Dynamics, 4(3), 251-259.

Smith, T., Ponzo, F. C., Di Cesare, A., Pampanin, S., Carradine, D., Buchanan, A. H., & Nigro, D. (2014). Post-tensioned glulam beam-column joints with advanced damping systems: testing and numerical analysis. Journal of Earthquake Engineering, 18(1), 147-167.

Soong, T. T., & Spencer, B. F. (2002). Supplemental energy dissipation: state-of-the-art and state-of-the-practice. Engineering Structures, 24(3), 243-259.

Tremblay, R. (2002). Inelastic seismic response of steel bracing members.*Journal of Constructional Steel Research*, *58*(5), 665-701.

Trombetti, T., Silvestri, S., Gasparini, G., & Ricci, I. (2009). Stiffness-Strength-Ductility-Design Approaches for Crescent Shaped Braces. Open Construction and Building Technology Journal, 3, 127-140.

Tsai, K. C., Chen, H. W., Hong, C. P., & Su, Y. F. (1993). Design of steel triangular plate energy absorbers for seismic-resistant construction. Earthquake spectra, 9(3), 505-528.

Uriz, P., Filippou, F. C., & Mahin, S. A. (2008). Model for cyclic inelastic buckling of steel braces. Journal of structural engineering, 134(4), 619-628.